Science Bulletin 64 (2019) 553–561

Contents lists available at ScienceDirect

Science Bulletin

journal homepage: www.elsevier.com/locate/scib

Science Bulletin
www.scibull.com

Article

Atomic pair distribution function research on Li_2MnO_3 electrode structure evolution

Yubo Yang [a,b], Heng Su [a], Tianhao Wu [a], Yuyuan Jiang [b], Danmin Liu [b,*], Pengfei Yan [b], Haolai Tian [c], Haijun Yu [a,*]

[a] College of Materials Science and Engineering, Key Laboratory of Advanced Functional Materials, Ministry of Education, Beijing University of Technology, Beijing 100124, China
[b] Institute of Solid State Microstructure and Properties, Beijing Key Laboratory of Microstructure and Property of Advanced Materials, Beijing University of Technology, Beijing 100124, China
[c] China Spallation Neutron Source, Dongguan Institute of Neutron Science, Institute of High Energy of Physics, Chinese Academy of Sciences, Dongguan 523803, China

ARTICLE INFO

Article history:
Received 18 February 2019
Received in revised form 5 March 2019
Accepted 11 March 2019
Available online 22 March 2019

Keywords:
Li-ion battery
Lithium-manganese-rich layered oxides
Local structure
Pair distribution function
Structure evolution

ABSTRACT

The mechanism research of structure-related reactions on Li_2MnO_3 is important to enhance the electrochemical performance of lithium-manganese-rich layered oxides. Although there are some reports on the structure evolution of Li_2MnO_3 during cycling process, the employed research techniques are very limited, mainly in/ex-situ X-ray diffraction, X-ray absorption and transmission electron microscopy. Here, atomic pair distribution function, a method to study the local atomic arrangement on the basis of average spectroscopic information, is used for the first time to study the local structure evolution of Li_2MnO_3 during electrochemical charge/discharge cycles. The results clearly demonstrate that Mn^{3+}/Mn^{4+} redox couple is activated and Mn ions are reduced during discharging process. Some Mn ions in Mn layers can significantly migrate to Li layers and occupy the octahedral sites. As a result, a portion of inserted Li ions can occupy the face-shared tetrahedron sites, accompanied by the formation of local spinel-like structure. This work provides an important and suitable method based on the average spectroscopic information to investigate the local structure of electrode materials of lithium-ion batteries as well as other advanced battery systems.

1. Introduction

With the increasing environmental issues (such as global warming and the emission of pollutants) from fossil fuels as well as their depletion, renewable and sustainable energy resources become urgent to our daily lives. Lithium-ion batteries (LIBs) are promising and environment-friendly energy devices, which have been extensively used in portable electronic devices and electric vehicles [1,2]. However, the energy density of commercialized LIBs is still unsatisfying to meet the needs of rapid development of new energy industry. There are two ways to increase the energy density of LIBs, including the lift of battery operating voltage and the enhancement of reversible capacity of electrode materials. Unfortunately, lack of electrolytes with wide voltage windows greatly limits the development of high-voltage LIBs. Therefore, most research works focused on the development of novel electrode materials with high reversible capacity [3,4].

Lithium-rich layered oxides (LLOs) are one of the most promising next-generation high-capacity LIB cathode materials [5,6]. They are believed to have complex "twin domain" structure consisting of Li_2MnO_3-like domain and layered $LiTMO_2$ (TM = transitional metals) domain, which are randomly distributed in the whole grain [7]. For LLOs used in LIBs, Li_2MnO_3 is the most important component and has received wide attentions [8,9]. First, Li_2MnO_3-like domain endows LLOs with high reversible capacity, usually exceeding 250 mAh/g in LIBs. Second, Li_2MnO_3-like domain is the key to induce the structure evolution of LLOs because of the existence of lithium and oxygen vacancies in the transitional metal layer during cycling process. In order to improve the electrochemical performance of LLOs, many efforts have been dedicated to stabilize their structures, such as surface coating [10] and element doping [11,12]. The fundamental understanding of structure evolution of Li_2MnO_3 is thus extremely important for improving the performance of LLO especially cyclability.

There have been some reports on the structure evolution of Li_2MnO_3. By using spherical aberration-corrected scanning transmission electron microscopy (STEM), the migration of Mn ions into the Li layer after electrochemical delithiation was demonstrated [13]. Based on X-ray absorption spectroscopy (XAS) and STEM techniques, the reduction of Mn ions during the initial discharge process in the low voltage region and the phase transition from

* Corresponding authors.
E-mail addresses: dmliu@bjut.edu.cn (D. Liu), hj-yu@bjut.edu.cn (H. Yu).

https://doi.org/10.1016/j.scib.2019.03.019
2095-9273/

monoclinic C2/m to tetragonal $I4_1$ and cubic spinel could also be confirmed [14–16]. Furthermore, with the assistance of in-situ high-energy X-ray diffraction (HEXRD) technique, it has been confirmed that Mn ions migrate from the octahedral sites to tetrahedral sites at elevated temperatures, a key step for the phase transformation from layered to spinel structure [17].

Among those analysis techniques, XRD is able to acquire the average structure information, (S)TEM is often used to provide the local structure information, and XAS is mainly used to investigate the change of valence state. However, it is crucial to understand more detailed information about the local structure directly from the average perspective. Atomic pair distribution function (PDF) is a method to analyze the atomic arrangement information in local regions based on the average structure information, which is convenient in terms of signal acquisition and can be analyzed contrastively with X-ray and neutron sources.

In this work, the structure evolution process and associated reaction mechanism of Li_2MnO_3 electrode were deeply investigated using PDF for the first time. In-situ XRD was also employed to systemically study the local and average structure evolution of the material during cycling process. Both the migration phenomenon of Mn ions and the occupancy information associated with structure evolution are elucidated. This work provides a new visual angle to study the local structure and structure evolution process of electrode materials for various battery systems, which plays an important role in understanding their reaction mechanisms.

2. Materials and methods

2.1. Preparation of materials

$MnCO_3$ precursor was first prepared by the precipitation method. Typically, $MnSO_4$ (2.0 mol/dm^3, Aladdin, 99.9%) and Na_2CO_3 (2.0 mol/dm^3, Aladdin, 99.9%) solutions were mixed simultaneously during stirring and the pH was controlled within 7–8 throughout. After the completion of the precipitation reaction, the resulted suspension was collected and washed with distilled water several times until the washing solution became neutral with a pH of 7. The obtained $MnCO_3$ precipitate was then dried in a vacuum oven at 80 °C for 12 h.

To synthesize Li_2MnO_3, $MnCO_3$ and Li_2CO_3 (Alfa Aesar, 99.9%) were mixed in a molar ratio of 100:101 and milled together with ethanol using a ball milling machine. The 1% excess of Li_2CO_3 was used to compensate the evaporation-induced Li loss during high-temperature sintering. The product was dried, calcined in air at 450 °C for 48 h and then at 500 °C for 12 h, and the Li_2MnO_3 material was obtained as an orange powder.

2.2. Battery fabrication and electrochemical test

Electrochemical tests were performed on 2032-type coin cells assembled with Li_2MnO_3 cathode and lithium foil anode. The cathode was made by laminating Al foil current collectors with a slurry containing the synthesized Li_2MnO_3 powder, conductive acetylene black and polyvinylidene fluoride (PVDF) binder in a weight ratio of 80:15:5 dispersed in N-methyl-2-pyrrolidone (NMP). Li_2MnO_3 powder and acetylene black were premixed with a mortar and pestle for 30 min before dispersed in the PVDF solution in NMP. The electrolyte was a 1 mol/L solution of $LiPF_6$ dissolved in mixed solvent of ethylene carbonate (EC) and ethyl methyl carbonate (EMC) in a volume ratio of 3:7 for all cells. Galvanostatic charge and discharge measurements were carried out in the voltage range of 2–4.8 V vs. Li^+/Li at a current density of 10 mA/g using a multichannel battery test system (LAND) at room temperature. To collect the cathode samples at different charge/discharge states for the ex-situ PDF test, the coin cells were kept at target voltages during charging for at least 12 h, or discharged to the selected voltages and calibrated the voltage every one hour for at least 12 times. Cyclic voltammetry (CV) measurements on the cells were performed with a Solartron electrochemical workstation in the potential range of 2–4.8 V at a scan rate of 0.1 mV/s.

2.3. Ex-situ PDF test

The atomic PDF provides atomic-scale structural insights from the distribution of atom–atom distance ranging from the local coordination scale to several nanometers as shown as the Fig. 1. The atomic PDF, $G(r)$ [18], can be defined as

$$G(r) = 4\pi r[\rho(r) - \rho_0],$$

where ρ_0 is the average atomic number density, $\rho(r)$ is the atomic pair-density defined below and r is the radial distance. The function $G(r)$ gives information about the number of atoms in a spherical shell of unit thickness at a distance r from a reference atom. The $G(r)$ can be calculated directly from a structural model using

$$G(r) = \frac{1}{r}\sum_i \sum_j \left[\frac{b_i b_j}{\langle b\rangle^2}\delta(r - r_{ij})\right] - 4\pi r\rho_0,$$

where the sum goes over all pairs of atoms i and j within the model crystal separated by r_{ij}. The scattering powers of atom i and the sample (average value) are termed as b_i and $<b>$, respectively. In the case of X-ray, the scattering power is the atomic forming factor evaluated at a given value of Q. The r_{ij} is the distance between the i^{th} and j^{th} atoms, and the sum is based on all the atoms in the sample.

Meanwhile, $G(r)$ is also an experimentally accessible function. It is related to the measured X-ray or neutron powder diffraction pattern through a Fourier transform

$$G(r) = \frac{2}{\pi}\int_{Q=0}^{Q_{max}} Q[S(Q) - 1]\sin(Qr)dQ,$$

where the total scattering structure function $S(Q)$ contains the measured diffraction intensity from an isotropic sample. Q is the scattering vector which is defined as

$$Q = 4\pi\sin\theta/\lambda.$$

Ex-situ PDF data were collected in the transmission mode at our laboratory using a Bruker D8 Advanced diffraction machine with a silver source (λ = 0.59 Å) operated at 50 kV and 20 mA. The collection angel was from 5° to 120°, while the upper Q-range can reach to 19 Å^{-1}. The testing sample of each state was acquired from four or five cycled coin cells, scraped down from the Al foil current collector and sealed in a capillary with Methacrylate (ab glue). All the processes were operated in an Ar glove box (H_2O and O_2 contents are below 0.1 ppm).

2.4. XRD and in-situ XRD measurement

The powder XRD pattern between 15° and 125° was collected using the Bruker D8 Advance Diffractometer using Cu Kα radiation with a scanning rate of 1°/min and step length of 0.02°. In-situ battery was assembled using a stainless steel cell with a Be window. The cathode material was laminated on ultra-thin Al foil as cathode, while metallic lithium foil was used as anode. In-situ XRD patterns of LIBs were collected on the Bruker D8 Advance Diffractometer for the initial three cycles with 2θ values ranging from 15° to 51° at a scanning rate of 10°/min when the battery was cycled with a current density of 15 mA/g.

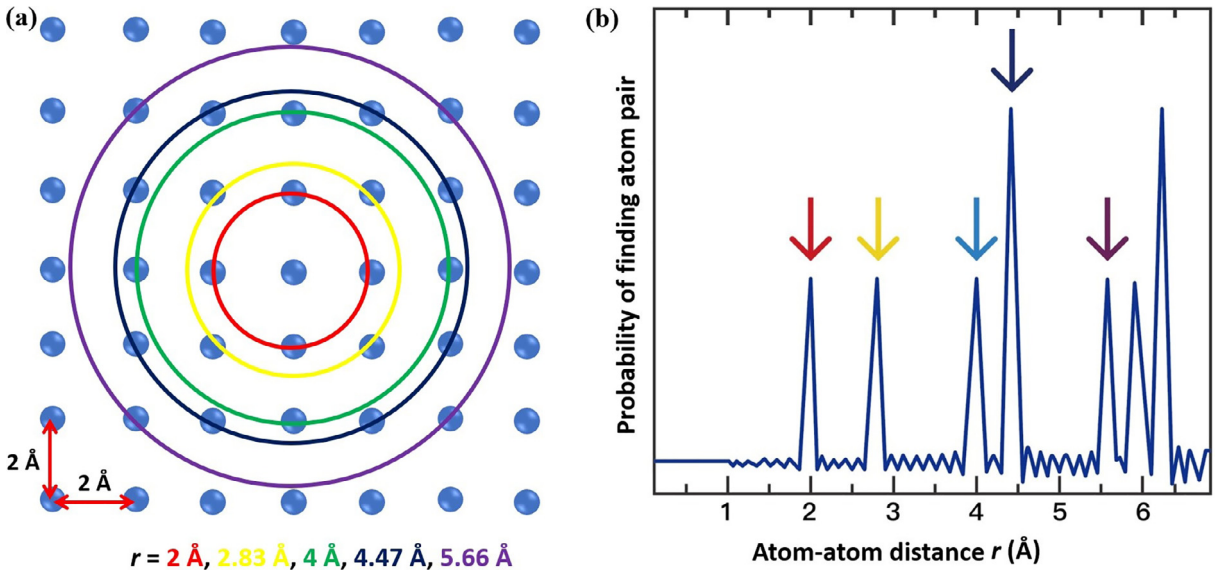

Fig. 1. (Color online) Schematic illustration for pair distribution function (PDF). (a) Atoms arrangement; (b) The corresponding PDF pattern.

2.5. HAADF-STEM and SEM

STEM investigation was conducted with a beam current of 60 pA on a FEI Titan 80–300 TEM with a probe corrector. SEM for the sample was performed on Hitachi S-4800 equipment to investigate their morphological characteristics.

3. Results and discussion

XRD and Rietveld refinement results of the as-synthesized Li_2MnO_3 are shown in Fig. 2a. All peaks are indexed to a typical monoclinic layer structure (ICDD PDF #04-011-3411) with C2/m space group. The results agree well with the PDF data, as shown in Fig. 2b. Both the XRD and PDF patterns have been refined using the same Li_2MnO_3 model with C2/m space group. In this structure, 1/4 lithium and manganese ions occupy the 2b and 4g sites of the Mn layer between ABC stacking sequence of oxygen layers, respectively. The rest lithium ions are located in the octahedral sites between Mn layers, as shown in the inset of Fig. 2a. Note that there are (0 2 0) and (1 1 0) diffraction peaks between 20° and 25°, indicating the ordered occupation of lithium ions in the Mn layer. All peaks exhibit a broadness character, demonstrating a large amount

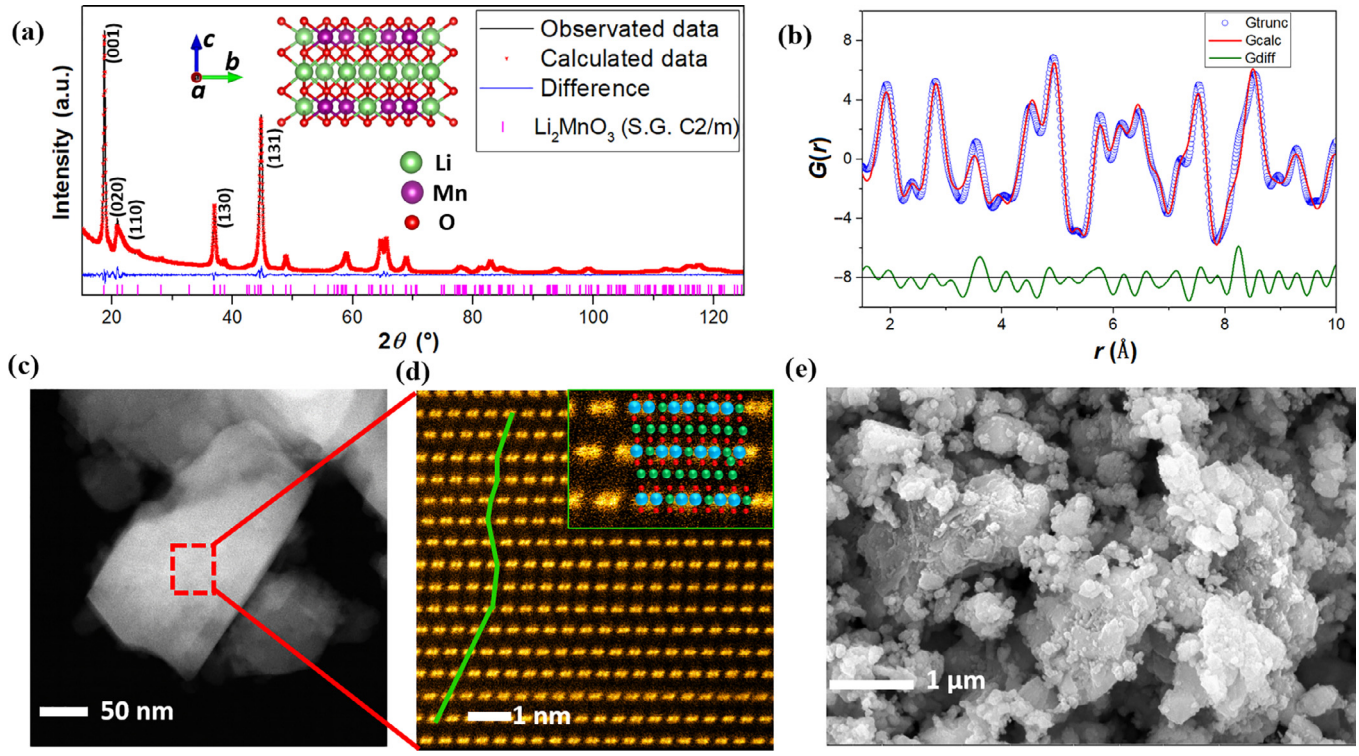

Fig. 2. (Color online) Structure and morphology characterization of the as-synthesized pristine Li_2MnO_3. (a) Rietveld refinement results for Li_2MnO_3. The inset image is the crystal structure of Li_2MnO_3 along the *a* axis direction. (b) The corresponding refined PDF pattern. (c) HAADF-STEM image of a single particle. (d) HADDF-STEM image shows the stacking faults between (0 0 1) planes (highlighted by green lines). Inset image: the enlarged HAADF-STEM image, which can match the ball model of Li_2MnO_3 very well. (e) The corresponding SEM image.

of stacking faults and Li/Mn atomic mixing in the Mn layer [19]. Rietveld refinement results are listed in Table 1, showing that there is around 25.9% atomic mixing between 2b and 4g sites of the Mn layer. Fig. 2c and d show the HAADF-STEM images of the Mn layer (Li–Mn–Mn) in Li_2MnO_3. The existence of a lot of stacking faults along the c axis as marked by the green line in Fig. 2d, agrees well with the above XRD and Rietveld Refinement results. Fig. 2e shows that the average size of as-synthesized Li_2MnO_3 particles is around 200 nm.

In order to understand the structure evolution of Li_2MnO_3 during cycling process, its electrochemical performance was tested at a current density of 10 mA/g between 2 and 4.8 V in a half cell configuration with Li foil as the anode. As shown in Fig. 3, the initial charge capacity is as high as 330 mAh/g with an obvious charge plateau at ~4.5 V vs. Li^+/Li. This large voltage plateau (Fig. 3a) disappears in the subsequent cycles, which is believed to be associated with the structure arrangement induced by Li_2MnO_3 activation and oxygen redox reaction [20–22]. Fig. 3b shows the CV curves of the Li_2MnO_3 cathode recorded between 2 and 4.8 V. In the first cycle, only one oxidation peak corresponding to the Li_2MnO_3 activation can be observed at around 4.6 V. After the first charge process, the oxidation and reduction peaks can be observed at 3.1 and 2.6 V, respectively, corresponding to the Mn^{3+}/Mn^{4+} redox couple [15,23,24]. Note that the oxidation peak at 4.6 V was very high in the first cycle and almost disappeared from the third cycle. It suggests the existence of partially irreversible reaction, probably associated with the oxygen redox reaction and in good agreement with the charge/discharge capacity evolution. The cycle performance of this material is shown in Fig. 3c. After 50 cycles, the capacity retention is only 9%. Such a poor cycling performance of this material, however, is useful to efficiently monitor the structure evolution for revealing the structure-performance relationship.

In-situ XRD technique is employed to examine the average structure evolution of Li_2MnO_3 during cycling process. The 2D contour plot of in-situ XRD patterns collected from 15° to 51° and the corresponding charge/discharge profiles of initial three cycles are presented in Fig. 4a and b, respectively. Peaks located at

Table 1
Rietveld refinement results. Li_2MnO_3 (space group C2/m), a = 4.9325(1) Å, b = 8.5360(0) Å, c = 5.0225(1) Å, β = 109.385(9)°, V = 199.477(2) Å^3, Rwp = 5.25%, and S = 1.22.

Atom	Site	x	y	z	Occupation	B
Li1	2b	0	0.5	0	0.740(1)	0.2208
Mn2	2b	0	0.5	0	0.259(9)	0.2208
Mn1	4g	0	0.1760(8)	0	0.480(2)	0.28
Li12	4g	0	0.1760(9)	0	0.519(8)	0.28
Li3	2c	0	0	0.5	1	0.9519
Li4	4h	0	0.6734(7)	0.5	1	0.9558
O1	4i	0.2420(3)	0	0.2148(2)	1	0.396
O2	8j	0.2468(5)	0.3207(7)	0.2387(2)	1	0.3793

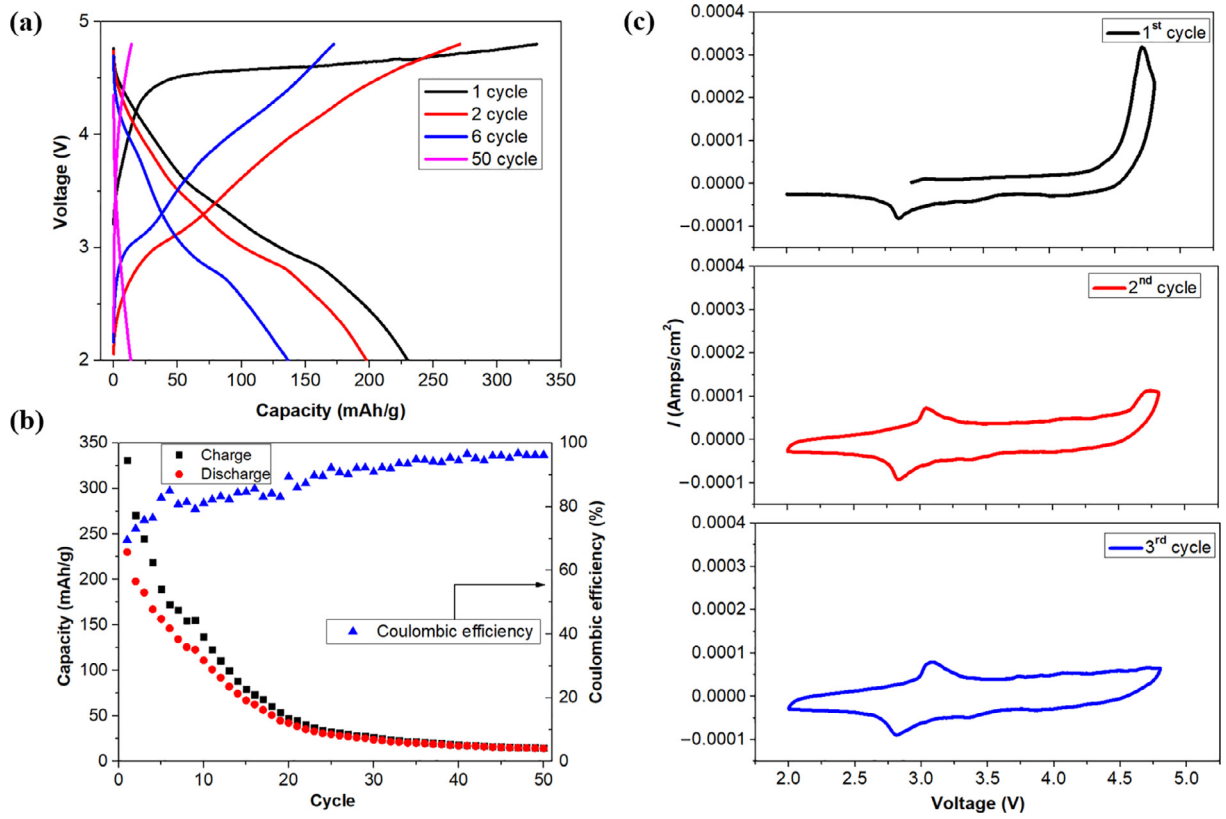

Fig. 3. (Color online) Electrochemical performance of the as-synthesized Li_2MnO_3. (a) Voltage profiles; (b) The coulombic efficiency, charge and discharge specific capacities during cycling in the voltage range of 2.0–4.8 V; (c) CV plots of the initial three cycles.

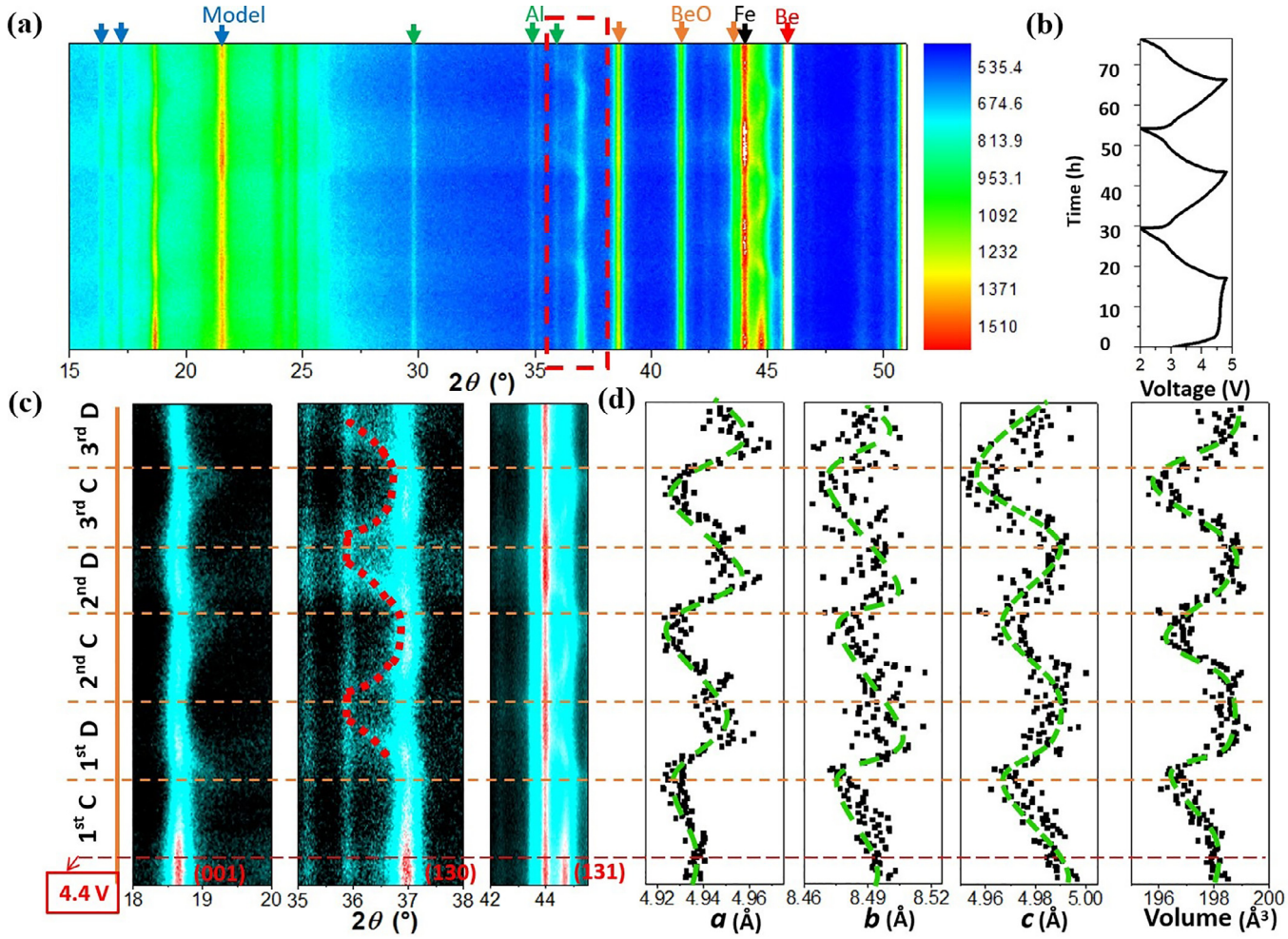

Fig. 4. (Color online) In-situ XRD analysis of the initial three cycles. (a) Whole contour plot of in-situ XRD. (b) The time–voltage plot at a current density of 15 mA/g. (c) Selected area in-situ XRD patterns; (d) Lattice parameters evolution of *a*, *b*, *c* and volume obtained by the fitted results of in-situ XRD. The peaks of stainless steel model, Al foil, BeO and Be are labeled above the contour plot. Different charge and discharge states are separated by dotted lines in (c) and (d).

21.6°/24.8°/44°, 29.8°/34.9°/36.2° and 38°/41.4°/42.6°/45.5° belong to the stainless steel model, Al current collector and Be window, respectively. The evolution of (0 0 1), (1 3 0) and (1 3 1) peaks of Li_2MnO_3 are shown in the enlarged patterns in Fig. 4c. Obviously, (0 0 1) and (1 3 0) peaks shift to higher angle region when the charge voltage is above 4.4 V, resulting from the shrink of lattice parameters *a*, *b* and *c* (Fig. 4d). Such a lattice shrink is likely originated from the oxygen loss and lattice densification during the charge process [25,26], which can also cause the obvious intensity weakening of Bragg peaks. In addition, it is noted that a new spinel (0 0 4) peak located at around 36.5° gradually appears during the initial discharge process, which cannot fully disappear during subsequent cycles. Moreover, this peak shifts to lower angle during the discharge process as marked by the red dot line in Fig. 4c, and reverse back upon the next charge process. These results suggest the formation of spinel-$LiMn_2O_4$ during the initial discharge process and a portion of Li ions can reversibly insert/extract into/from the spinel structure [24,27–29]. In addition, the intensity of the spinel-$LiMn_2O_4$ peak grows upon the further cycling, demonstrating the continuous structure transformation from layered to spinel, a process always accompanied by the migration of Mn ions from the Mn layer to the Li layer [16,28,30]. From all these changes of lattice parameters during the initial three cycles in Fig. 4d, it is clearly concluded that the evolution of Li_2MnO_3 is partially reversible.

Average structure changes can be derived from the in-situ XRD patterns. In order to further understand the atomic arrangement and the mechanism of the formation of spinel structure, ex-situ PDF measurement was conducted to express the local structures from an average perspective. Five charge/discharge states in the first cycle (charged to 4.4, 4.6 and 4.8 V, and discharged to 3.2 and 2 V) were collected as shown in Fig. 5a. These data were further analyzed by PDFGetX3 (version 1.1) [31] as shown in Fig. 5b. Four peaks located at 1.92, 2.83, 4.53 and 4.92 Å can be assigned to the nearest Mn—O bond, the nearest Mn—Mn bond, the third coordination Mn—O bond and the sub-neighboring distance of Mn—Mn bond, respectively, as shown in Fig. 5c and d. For clarity, these bonds are donated as Mn—O_I (1.92 Å), Mn—Mn_I (2.83 Å), Mn—O_{II} (4.53 Å) and Mn—Mn_{II} (4.92 Å), respectively. During the overall charge/discharge process in the first cycle, Mn—O_I peak keeps static, suggesting the good stability of MnO_6 octahedron. The Mn—O_{II} peak and Mn—Mn_{II} peak originate from intralayer bonds and the two bonds mainly reflect the layer structure. It is obvious that both peaks shift to the lower distance region during charging and reverse back during discharging, suggesting the lattice parameters can shrink and recover in the two processes, respectively. The results agree well with the in-situ XRD experimental data. A PDF peak ($r \approx 3.5$ Å) of pristine sample in Fig. 5b corresponds to the second coordination Mn—O bond labeled by pink double arrows dash line in Fig. 5c, and it is weak due to the

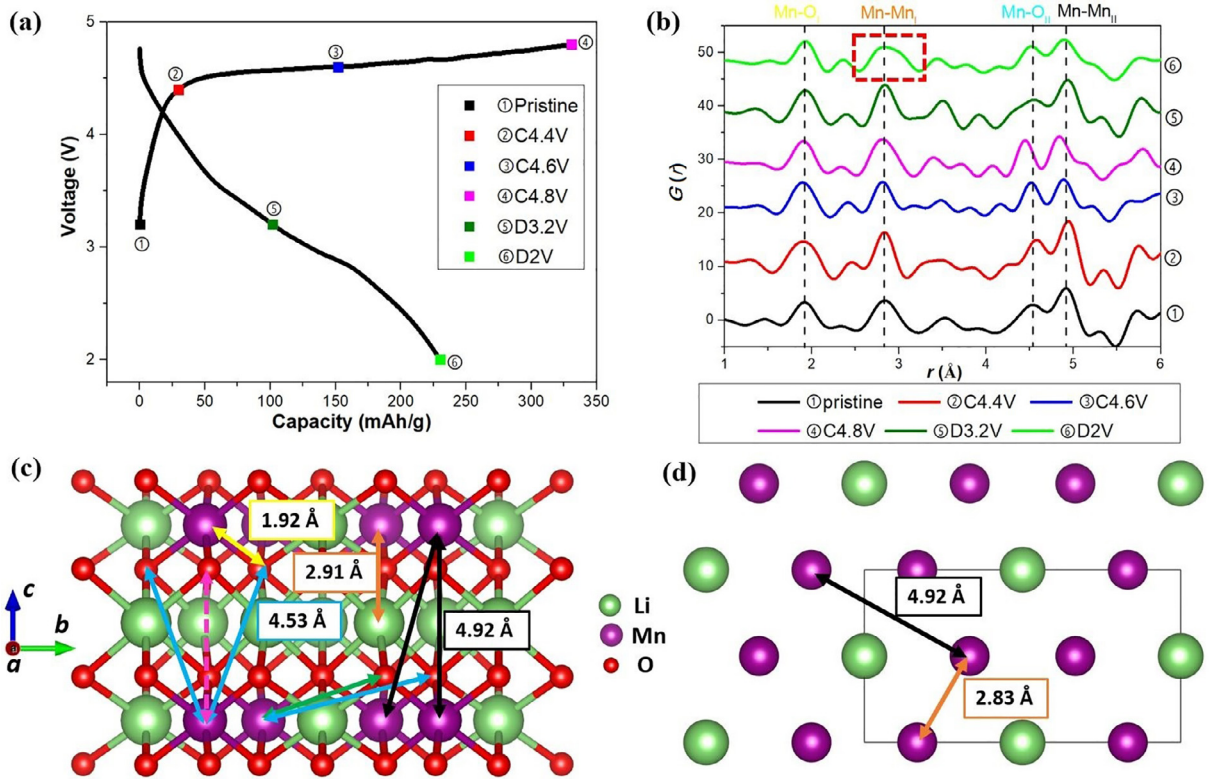

Fig. 5. (Color online) Atomic PDF evolution of the first cycle. (a) Charge and discharge profiles of the first cycle for Li_2MnO_3. (b) Corresponding PDF pattern at different charge/discharge states. (c) Crystal structure of Li_2MnO_3 along *a* axis and (d) atom arrangement of Mn layers.

low coordination number of the bonds. Thus, it has a very low signal-to-noise ratio and its evolution could not be displayed. Note that the Mn—Mn$_I$ peak broadens at the fully discharge state, and seems to split into two peaks. Two possible reasons may explain this phenomenon, (1) a part of Mn ions were reduced during the discharge process, leading to the increase of their radius, and (2) a portion of Mn ions may migrate to the Li layer and occupy the Li site, as supported by the Mn—Li bond distance of 2.91 Å in Fig. 5c.

To further verify this proposal, ex-situ PDF measurements at fully discharge states from 1st, 2nd, 6th and 50th cycles were also conducted as shown in Fig. 6a. Mn—O$_I$ peak shows no movement after 50 cycles, suggesting MnO_6 octahedrons are stable. However, Mn—Mn$_I$ peak gradually shifts to 2.91 Å, in good agreement with the distance of Mn—Li bond in the Li_2MnO_3 lattice, indicating that Mn ions may partially migrate to the Li layer and occupy the Li-ion sites. Mn—O$_{II}$ peak obviously shifts to the lower distance region while Mn—Mn$_{II}$ peak shifts to the higher distance region after 50

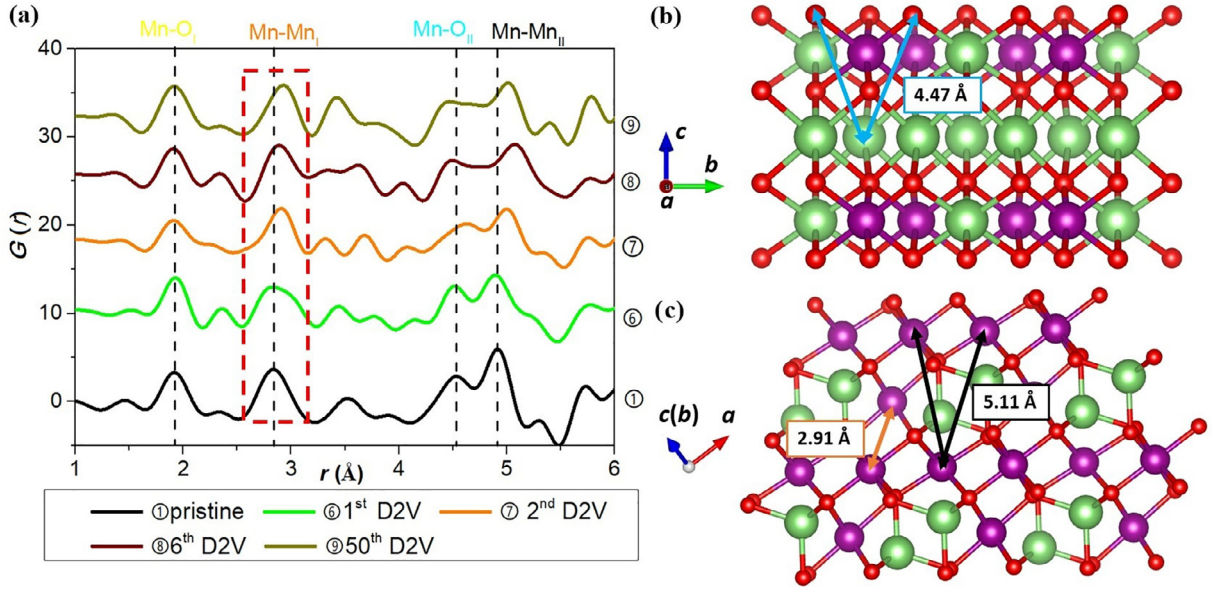

Fig. 6. (Color online) Atomic PDF evolution of discharging states. PDF patterns for Li_2MnO_3 at different cycle states (a). Crystal structure of layered structure (b) and spinel structure (c).

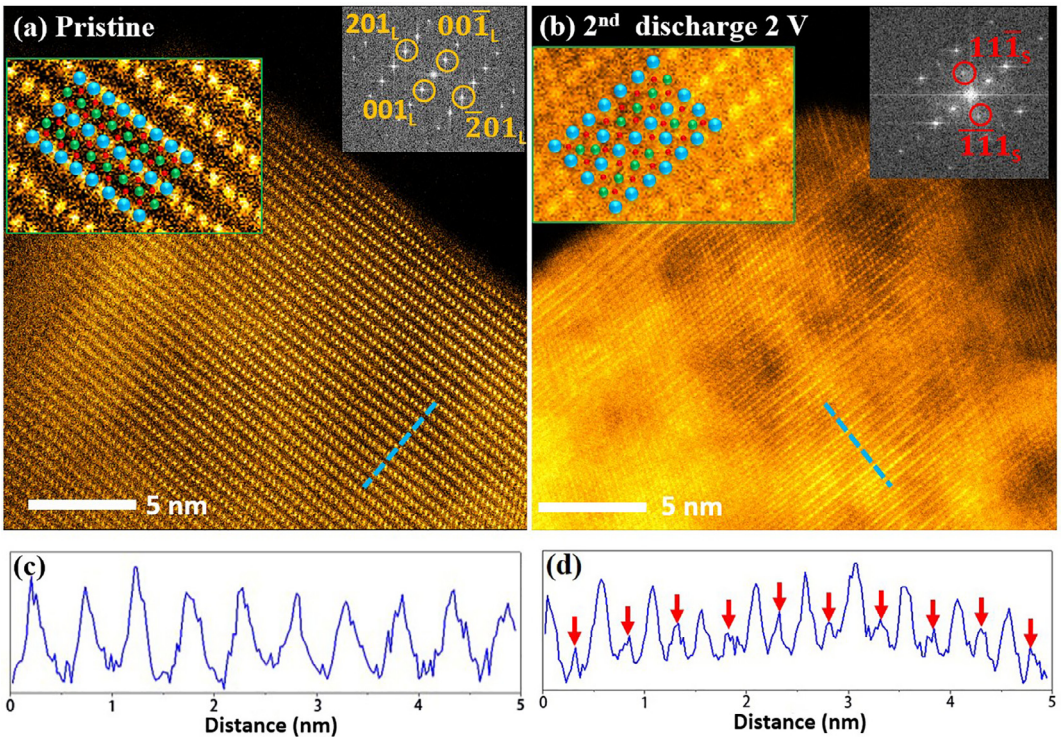

Fig. 7. (Color online) Characterization of STEM. HAADF-STEM images of pristine state (a) and the second discharge 2 V state (b). Inset image in (a) and (b) are enlarged images of HAADF-STEM and corresponding FFT results, respectively. (c), (d) Corresponding scan intensity of the blue dotted lines in (a) and (b), respectively.

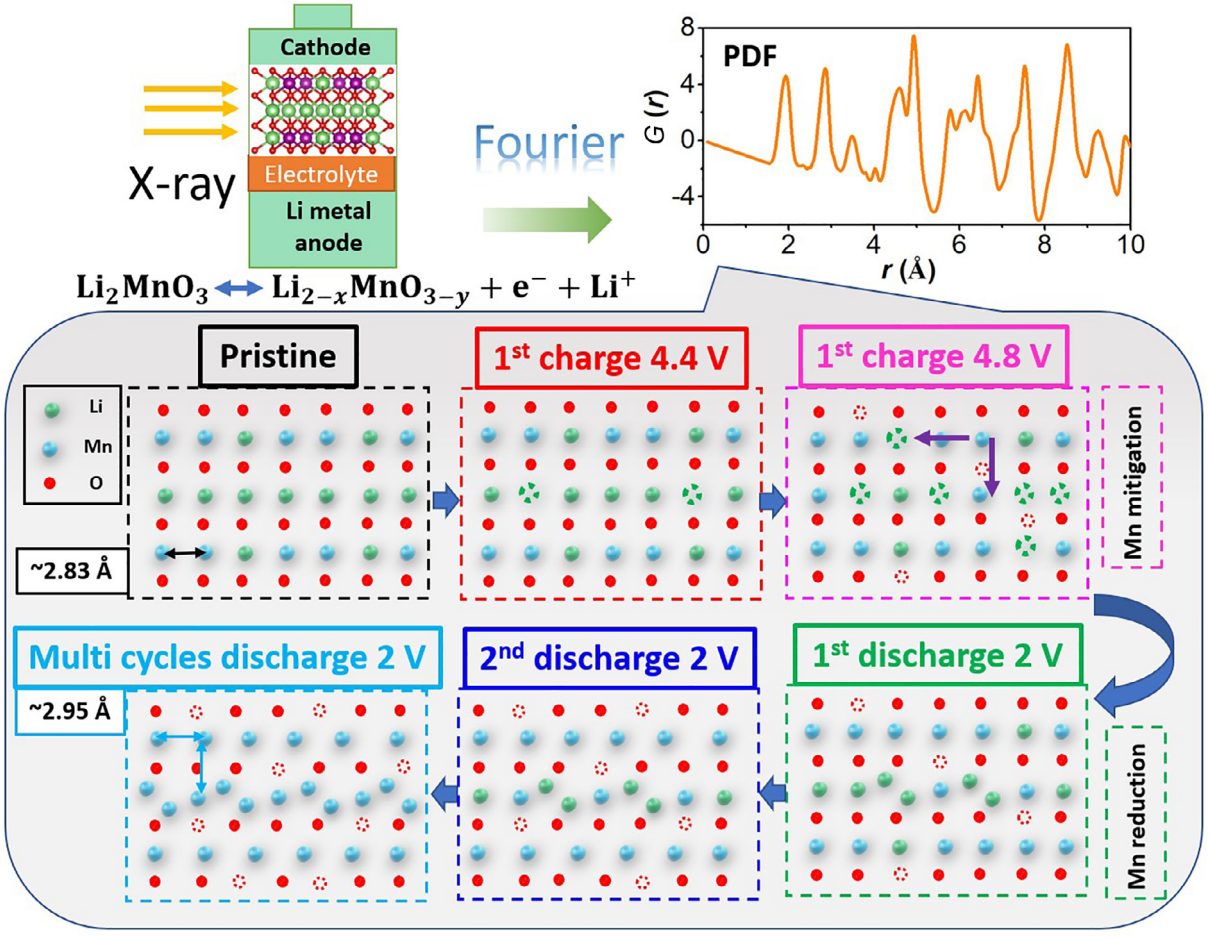

Fig. 8. (Color online) Schematic illustration of Li_2MnO_3 structure evolution during the first cycle and subsequent cycles.

cycles. As can be more clearly seen in Fig. 6b, the distance of Li—O_{II} (labeled by blue double arrows line) is 4.47 Å, suggesting that Mn ions migrate to the Li vacant sites in the Li layer during cycling and cannot fully return to the Mn layer. Fig. 7 shows the HAADF-STEM images of cathode materials at pristine state (Fig. 7a) and discharged state from the second cycle (Fig. 7b). At the pristine state, the layer structure is clear and the projections of Mn ions rank continuously along *a* axis of Li_2MnO_3. However, after two cycles, the distribution of Mn ions is somewhat ambiguous, and even some dark shadow areas appear, which may be related to the corrosion effect of electrolyte or irradiation damage of electron beam [16,28,32]. Line scans of HAADF intensity along *c* axis for these two states are shown in Fig. 7c and d, respectively. Obviously, Mn ions migrate to Li layers according to the new peaks labeled by red arrows in Fig. 7d. The results further confirm that Mn ions can migrate to the Li vacancy in Li-layer during the cycling process, and cannot fully return to the Mn layer.

We have calculated all the Mn—Mn_{II} and Li—Mn_{II} bonds in the Li_2MnO_3 crystal lattice. However, there is no bond matching with the shifting of Mn—Mn_{II} peak in Fig. 6a. As shown in Fig. 4, a spinel-like structure phase generates during the cycling process and grows gradually upon cycling. Thus, the Mn—Mn bonds of spinel lattice were also calculated. As shown in Fig. 6c, the distance of Mn—Mn_{II} bond in the spinel lattice is 5.11 Å, which perfectly matches with the shift of Mn—Mn_{II} peak in Fig. 6a. The results demonstrate that Mn ions mitigate to the Li vacancy in the Li layer with the formation of the spinel-like structure phase.

Overall, as shown in Fig. 8, the structure evolution of Li_2MnO_3 during the cycling process were measured and analyzed by PDF technique. The pristine material exhibits a typical monoclinic layer structure, in which 1/4 lithium and manganese ions respectively occupy the 2b and 4g sites in the Mn layer. The rest lithium ions are located in the octahedral sites between Mn layers (black dashed rectangle in Fig. 8). When firstly charged below 4.4 V, Li ions in the Li layer partly extract from the structure while Li ion in the Mn layer keep stable (red dashed rectangle in Fig. 8). When further charged to 4.8 V, Li ions in the Li layer begin to extract from the structure, accompanied by the oxygen redox reaction and lattice densification (pink dashed rectangle in Fig. 8). During this process, a small portion of Mn ions in the Mn-layer significantly migrate to the Li layer and occupy the octahedral sites. After firstly discharged to 2.0 V, Mn^{3+}/Mn^{4+} redox couple is activated and Mn ions are reduced. Meanwhile, part of inserted Li ions may occupy the face-shared tetrahedron sites in the Li layer, accompanied by the formation of spinel-like structure in the local structure (green dashed rectangle in Fig. 8). In the subsequent cycles, the phase ratio of spinel-like structure will be constantly increased, which may result in the decline of reversible capacity for Li_2MnO_3 material.

4. Conclusions

In summary, Li_2MnO_3 was synthesized by a conventional solid state reaction method. It delivers a high charge capacity of 330 mAh/g and discharge capacity of ~230 mAh/g. The mechanism of its structure evolution during cycling process is firstly studied by the atomic PDF technique and the local structure information based on average perspective is obtained. A new spinel (0 0 4) peak gradually appears during the charging process and grows with further cycling, demonstrating that the spinel transformation gradually takes place. Further investigation on its local structure indicates that Li ions in the Mn layer extract from the structure above 4.4 V (vs Li/Li^+), accompanied by the oxygen redox reaction and lattice densification. The Mn^{3+}/Mn^{4+} redox couple is activated and Mn ions are reduced during the discharging process. A small portion of Mn ions in the Mn layer significantly migrate to the Li layer and occupy the octahedral sites. As a result, a part of the inserted Li ions occupy the face-shared tetrahedron sites with the formation of spinel-like structure in local structure. Moreover, the ratio of spinel-like phase is constantly increased with the subsequent cycle process.

Conflict of interest

The authors declare that they have no conflict of interest.

Acknowledgments

This work was supported financially by the Beijing Natural Science Foundation (B) (KZ201610005003), National Natural Science Foundation of China (51622202, U1507107, 21603009 and 51802009), National Key R&D Program of China (2018YFB0104302) and Guangdong Science and Technology Project (2016B010114001).

Author contributions

Haijun Yu conceived and designed this work. Yubo Yang performed the PDF experiments and wrote the manuscript. Tianhao Wu performed the in-situ XRD experiment. Yuyuan Jiang and Pengfei Yan performed the TEM experiments. Haijun Yu and Heng Su revised the manuscript. Danmin Liu and Haolai Tian discussed the manuscript. All authors participated in analyzing the experimental results and preparing the manuscript.

References

[1] Armand M, Tarascon JM. Building better batteries. Nature 2008;451:652–7.
[2] Whittingham MS. Ultimate limits to intercalation reactions for lithium batteries. Chem Rev 2014;114:11414–43.
[3] Goodenough JB, Kim Y. Challenges for rechargeable batteries. J Power Sources 2011;196:6688–94.
[4] Cho E, Kim K, Jung C, et al. Overview of the oxygen behavior in the degradation of Li_2MnO_3 cathode material. J Phys Chem C 2017;121:21118–27.
[5] Yu H, Kim H, Wang Y, et al. High-energy "composite" layered manganese-rich cathode materials via controlling Li_2MnO_3 phase activation for lithium-ion batteries. Phys Chem Chem Phys 2012;14:6584–95.
[6] Manthiram A, Knight JC, Myung ST, et al. Nickel-rich and lithium-rich layered oxide cathodes: progress and perspectives. Adv Energy Mater 2016;6:1501010.
[7] Yu H, So YG, Kuwabara A, et al. Crystalline grain interior configuration affects lithium migration kinetics in Li-rich layered oxide. Nano Lett 2016;16:2907–15.
[8] Hy S, Liu H, Zhang M, et al. Performance and design considerations for lithium excess layered oxide positive electrode materials for lithium ion batteries. Energy Environ Sci 2016;9:1931–54.
[9] Zheng J, Myeong S, Cho W, et al. Li- and Mn-rich cathode materials: challenges to commercialization. Adv Energy Mater 2017;7:1601284.
[10] Zhang XD, Shi JL, Liang JY, et al. Suppressing surface lattice oxygen release of Li-rich cathode materials via heterostructured spinel $Li_4Mn_5O_{12}$ coating. Adv Mater 2018;30:1801751.
[11] Nayak PK, Grinblat J, Levi M, et al. Al doping for mitigating the capacity fading and voltage decay of layered Li and Mn-rich cathodes for Li-ion batteries. Adv Energy Mater 2016;6:1502398.
[12] Zubair M, Wang B, Li G, et al. Electrochemical kinetics and cycle stability improvement with Nb doping for lithium-rich layered oxides. ACS Appl Energy Mater 2018;2:503–12.
[13] Wang R, He X, He L, et al. Atomic structure of Li_2MnO_3 after partial delithiation and re-lithiation. Adv Energy Mater 2013;3:1358–67.
[14] Croy JR, Park JS, Dogan F, et al. First-cycle evolution of local structure in electrochemically activated Li_2MnO_3. Chem Mater 2014;26:7091–8.
[15] Oishi M, Yamanaka K, Watanabe I, et al. Direct observation of reversible oxygen anion redox reaction in Li-rich manganese oxide, Li_2MnO_3, studied by soft X-ray absorption spectroscopy. J Mater Chem A 2016;4:9293–302.
[16] Yan P, Xiao L, Zheng J, et al. Probing the degradation mechanism of Li_2MnO_3 cathode for Li-ion batteries. Chem Mater 2015;27:975–82.
[17] Kan Y, Hu Y, Lin CK, et al. Migration of Mn cations in delithiated lithium manganese oxides. Phys Chem Chem Phys 2014;16:20697–702.
[18] Egami T, Billinge S. Underneath the Bragg Peaks. 2nd ed. Pergamon; 2012.
[19] Matsunaga T, Komatsu H, Shimoda K, et al. Dependence of structural defects in Li_2MnO_3 on synthesis Temperature. Chem Mater 2016;28:4143–50.

[20] Seo DH, Lee J, Urban A, et al. The structural and chemical origin of the oxygen redox activity in layered and cation-disordered Li-excess cathode materials. Nat Chem 2016;8:692–7.
[21] Luo K, Roberts MR, Hao R, et al. Charge-compensation in 3d-transition-metal-oxide intercalation cathodes through the generation of localized electron holes on oxygen. Nat Chem 2016;8:684–91.
[22] Luo K, Roberts MR, Guerrini N, et al. Anion redox chemistry in the cobalt free 3d transition metal oxide intercalation electrode $Li[Li_{0.2}Ni_{0.2}Mn_{0.6}]O_2$. J Am Chem Soc 2016;138:11211–8.
[23] Robertson AD, Bruce PG. Mechanism of electrochemical activity in Li_2MnO_3. Chem Mater 2003;15:1984–92.
[24] Shimoda K, Oishi M, Matsunaga T, et al. Direct observation of layered-to-spinel phase transformation in Li_2MnO_3 and the spinel structure stabilised after the activation process. J Mater Chem A 2017;5:6695–707.
[25] Tran N, Croguennec L, Ménétrier M, et al. Mechanisms associated with the "plateau" observed at high voltage for the overlithiated $Li_{1.12}(Ni_{0.425}Mn_{0.425}Co_{0.15})_{0.88}O_2$ system. Chem Mater 2008;20:4815–25.
[26] Yu H, So Y-G, Ren Y, et al. Temperature-sensitive structure evolution of lithium-manganese-rich layered oxides for lithium-ion batteries. J Am Chem Soc 2018;140:15279–89.
[27] Kondracki Ł, Kulka A, Milewska A, et al. In-situ structural studies of manganese spinel-based cathode materials. Electrochim Acta 2017;227:294–302.
[28] Phillips PJ, Bareño J, Li Y, et al. On the localized nature of the structural transformations of Li_2MnO_3 following electrochemical cycling. Adv Energy Mater 2015;5:1501252.
[29] Amalraj SF, Burlaka L, Julien CM, et al. Phase transitions in Li_2MnO_3 electrodes at various states-of-charge. Electrochim Acta 2014;123:395–404.
[30] Mohanty D, Li J, Abraham DP, et al. Unraveling the voltage-fade mechanism in high-energy-density lithium-ion batteries: origin of the tetrahedral cations for spinel conversion. Chem Mater 2014;26:6272–80.
[31] Juhás P, Davis T, Farrow CL, et al. PDFgetX3: a rapid and highly automatable program for processing powder diffraction data into total scattering pair distribution functions. J Appl Crystallogr 2013;46:560–6.
[32] Phillips PJ, Iddir H, Abraham DP, et al. Direct observation of the structural and electronic changes of Li_2MnO_3 during electron irradiation. Appl Phys Lett 2014;105:113905.

Yubo Yang is a Ph.D. candidate at Beijing University of Technology under the supervision of Prof. Haijun Yu and Prof. Danmin Liu. His research interests are Li-rich materials for lithium-ion batteries.

Danmin Liu earned a Materials Science diploma at the Central South University of Technology in 1986 and then worked there. In 1994, she joined Beijing University of Technology (BJUT) and received her M.S. and Ph. D. degrees in 1999 and 2006, respectively. Since 2008, she has been a professor at the Institute of Microstructure and Property of Advanced Materials, BJUT. Her current research interests focus on the advanced functional materials.

Haijun Yu is currently a professor at College of Materials Science and Engineering, Beijing University of Technology (BJUT). He received his Ph.D. degree in 2007 from Northeastern University, and then did research work on advanced battery materials and devices at General Research Institute for Non-ferrous Metals (GRINM) and National Institute of Advanced Industrial Science and Technology (AIST). His current research interests focus on the advanced electrode materials for lithium/sodium/aluminum-ions batteries, all-solid-state batteries, novel devices for energy storage and reaction mechanism.